Enhancement of contact line mobility by means of infrared laser illumination

Document Version:
Publisher's PDF, also known as Version of Record (includes final page, issue and volume numbers)

Please check the document version of this publication:

• A submitted manuscript is the version of the article upon submission and before peer-review. There can be important differences between the submitted version and the official published version of record. People interested in the research are advised to contact the author for the final version of the publication, or visit the DOI to the publisher's website.
• The final author version and the galley proof are versions of the publication after peer review.
• The final published version features the final layout of the paper including the volume, issue and page numbers.
[Link to publication](#)

Enhancement of contact line mobility by means of infrared laser illumination. II. Numerical simulations

H. M. J. M. Wedershoven, M. A. van den Tempel, J. C. H. Zeegers, and A. A. Darhuber

---

Articles you may be interested in

Active microrheology of colloidal suspensions: Simulation and microstructural theory
J. Rheol. **60**, 733 (2016); 10.1122/1.4954201

Enhancement of contact line mobility by means of infrared laser illumination. I. Experiments
J. Appl. Phys. **119**, 084904 (2016); 10.1063/1.4941389

Relaxation processes in liquids: Variations on a theme by Stokes and Einstein
J. Chem. Phys. **138**, 12A526 (2013); 10.1063/1.4775741

Three-dimensional direct numerical simulation for film-boiling contact of moving particle and liquid droplet
Phys. Fluids **18**, 117104 (2006); 10.1063/1.2386027

Study of the Cooling Process of an Extruded Aluminium Profile
AIP Conf. Proc. **712**, 588 (2004); 10.1063/1.1766590

Enhancement of contact line mobility by means of infrared laser illumination. II. Numerical simulations

H. M. J. M. Wedershoven, M. A. van den Tempel, J. C. H. Zeegers, and A. A. Darhuber
Mesoscopic Transport Phenomena Group, Department of Applied Physics, Eindhoven University of Technology, Postbus 513, 5600 MB Eindhoven, The Netherlands

A droplet that moves on a solid substrate with a velocity higher than a certain critical velocity disintegrates, i.e., leaves behind residual droplets. Infrared laser illumination can be used to increase the droplet mobility and suppress the shedding of droplets. By means of two-dimensional numerical simulations, we studied the effect of a non-uniform temperature distribution on the dynamics of straight receding contact lines. A streamfunction-vorticity model is used to describe the liquid flow in the vicinity of the receding contact line. The model takes into account the thermocapillary shear stress and the temperature-dependent liquid viscosity and density. A second, coupled model describes the laser-induced displacement of the contact line. Our results show that the reduction of the liquid viscosity with increasing temperature is the dominant mechanism for the increase of the critical velocity. Thermocapillary shear stresses are important primarily for low substrate speeds. © 2016 AIP Publishing LLC. [http://dx.doi.org/10.1063/1.4941438]

I. INTRODUCTION

The motion of droplets moving along solid surfaces[1–9] is important for many technological applications. Usually, a high droplet mobility is desirable, which can be increased in various ways. Ogawa *et al.* and many others rendered substrates superhydrophobic.[10–13] Similar to lotus leaves, the liquid-solid interfacial area is substantially reduced, thereby only few degrees of inclination are sufficient to make a droplet slide.[10] A prominent application is self-cleaning surface coatings.[12] Smith *et al.* impregnated topologically patterned surfaces with lubricant oils in order to enhance the droplet mobility.[14] Other techniques for droplet mobilization include substrate vibrations[15,16] or A.C. electrowetting.[17] Many authors have studied droplet actuation by means of thermocapillary stresses as a consequence of localized heating[18–28] and specifically the effect of thermocapillary stresses on the dynamics of the moving contact lines.[29–36] If either the driving force or the imposed speed exceeds a critical limit, commonly residual liquid is left behind on the substrate.[37–44] Our study is motivated by immersion lithography, where the occurrence of such residual liquid is undesirable.[45,46]

In this manuscript, we study the increase of mobility of a stationary contact line on a moving, partially wetting substrate by means of localized infrared (IR) laser irradiation. In Paper I,[69] we presented corresponding experimental results. In the following, we present two coupled numerical models that allow us to identify the dominant mechanism of the mobility enhancement and to detail the influence of both thermocapillary shear stresses and viscosity reduction.

In the first model, we solve the coupled problem of heat-transfer and fluid flow near the receding contact line in a two-dimensional geometry. Anderson and Davis presented an analytical model accounting for heat conduction and the effect of thermocapillary stresses on the convection pattern.[34] Our numerical model, in addition, takes into account the convection

of heat as well as the effect of temperature induced reductions of density and viscosity. In the second model, the one-dimensional lubrication equation is solved to describe the contact line displacement in response to the thermocapillary stress and the variation of the liquid material properties. The stress singularity at the moving contact line is resolved using a disjoining pressure model.[47–51]

In Section II, the details of the two models are presented. Section III presents results from the heat-transfer model alone. In Section III, we consider the coupling between the two models. We study the dynamic receding contact angle as a function of substrate speed and laser power and determine the corresponding increase in critical velocity.

II. NUMERICAL MODELS

In order to study the effect of a non-uniform temperature distribution on a receding contact line, we couple a model for the heat-transfer in the vicinity of the contact line (CL) with a separate model for the displacement of the contact line. Figure 1 shows how the two models are coupled. First, we start with a certain receding contact angle θ_r and a certain distance between the contact line and the point of maximum
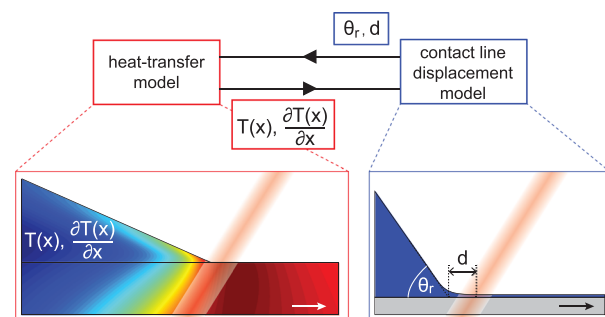

FIG. 1. Iteration diagram illustrating the coupling of the heat-transfer model and the contact line displacement model.

laser intensity, d. We then solve the heat-transfer model for the temperature distribution around the contact line. This temperature distribution is used in the contact line displacement model to update θ_r and d. The two models are solved iteratively until a self-consistent receding contact angle results. In Subsections II A–II C, the details of the two models are presented.

A. Heat-transfer model

Figure 2 shows the 2D computational domain for the thermal model. It consists of three separate geometries: the wedge represents a receding meniscus of ethylene glycol (EG), the upper rectangle the polycarbonate (PC) substrate, and the lower rectangle the glass plate. The coordinates $(x, y) = (0, 0)$ correspond to the receding contact line position. We assume that the shape of the liquid-air interface is given by a straight line, the slope of which is determined by the value of θ_r. The thickness of the PC substrate in the y-direction is $d_{PC} = 0.5$ mm and that of the glass plate $d_{glass} = 3.9$ mm. The height of the wedge at x_L is determined by the value of θ_r. The left boundaries of the three domains are located at $x_L = -16$ mm. The right boundaries of the PC substrate and the glass plate are located at $x_R = 16$ mm.

The steady-state temperature distribution $T(x,y)$ is described by the heat-transfer equation

$$\rho c_p \vec{u} \cdot \nabla T = k \nabla^2 T + \dot{q} . \tag{1}$$

The liquid velocity $\vec{u}$ in the EG wedge is calculated using a separate model, as outlined in Section II A 1. The PC substrate and the glass plate are moving in the x-direction with a constant velocity $\vec{u} = (U_{sub}, 0)$. The density ρ, specific heat capacity c_p, and thermal conductivity k of EG, PC, and glass are listed in Appendix B. The density of EG, $\rho(T)$, depends on the local temperature and is given by Eq. (B3) of Appendix B. The term $\dot{q} \equiv \alpha I$ represents a heat source due to absorption of the IR laser beam.[52–54] We assume the following IR absorption coefficients: $\alpha_{EG} = 700 \, \text{m}^{-1}$, $\alpha_{PC} = 30 \, \text{m}^{-1}$, and $\alpha_{glass} = 100 \, \text{m}^{-1}$. The intensity distribution $I(x,y)$ of the IR laser beam is discussed in Section II A 2.
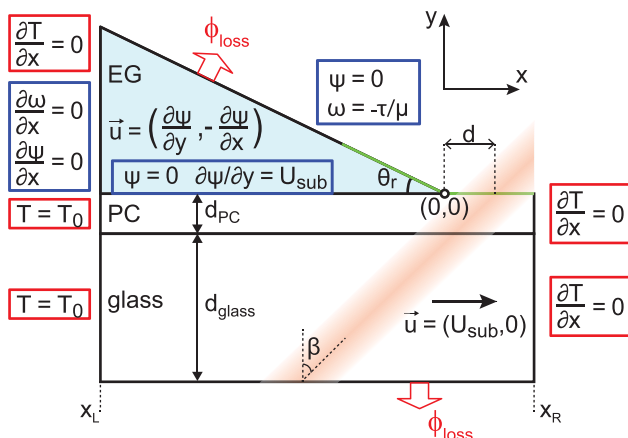

FIG. 2. Schematic representation of the computational domain and boundary conditions of the heat-transfer model (not to scale).

The initial condition is a uniform temperature $T_0 = 293$ K. The boundary conditions that we used are given by

$$\frac{\partial T}{\partial x}(x = x_L, y > 0) = 0, \tag{2}$$

$$\frac{\partial T}{\partial x}(x = x_R, y \leq 0) = 0, \tag{3}$$

$$T(x = x_L, y \leq 0) = T_0, \tag{4}$$

$$-k_{PC}\frac{\partial T}{\partial y}(x > 0, y = 0) = \phi_{loss}, \tag{5}$$

$$k_{glass}\frac{\partial T}{\partial y}(y = -d_{PC} - d_{glass}) = \phi_{loss}, \tag{6}$$

$$-\vec{n} \cdot k_{EG}\nabla T(x < 0, y = -\tan(\theta_r)x) = \phi_{loss}. \tag{7}$$

The temperature of the PC substrate and the glass plate at $x = x_L$ is kept at T_0 [Eq. (4)]. We assume that heat losses occur at the top boundary of the PC substrate (at $x > 0$), at the bottom boundary of the glass plate, and at the liquid-air interface [Eqs. (5), (6), and (7)], which are a superposition of Newtonian convective cooling and thermal radiation

$$\phi_{loss} = h_N(T - T_\infty) + \sigma_B(T^4 - T_\infty^4) . \tag{8}$$

Here, $h_N = 5 \, \text{W/(m}^2\text{ K)}$ is the convective heat transfer coefficient,[55] $\sigma_B = 5.67 \times 10^{-8} \, \text{W/(m}^2\text{ K}^4)$ the Stefan-Boltzmann constant, and $T_\infty = T_0 = 293$ K the ambient temperature. For the boundaries at $x = x_R$ and the boundary of the EG wedge at $x = x_L$, we use so-called convective boundary conditions [Eqs. (2) and (3)]. In the expression for the total heat flux $\vec{n} \cdot \vec{q} = (\rho c_p \vec{u} T - k\nabla T) \cdot \vec{n}$, we assume that the diffusive flux $-\vec{n} \cdot k\nabla T$ is negligible compared to the convective flux $\vec{n} \cdot \rho c_p \vec{u} T$ (where $\vec{n}$ is the unit normal vector of the computational domain).

1. Streamfunction-vorticity model

For the liquid velocity in the EG wedge, we estimate the typical values of the Reynolds number $Re_L = \frac{\rho L U_{sub}}{\mu} \leq 2$, where we use the maximum height of the wedge $L = x_L \tan(\theta_d) \approx 5$ mm and $U_{sub} \approx 5$ mm/s. Consequently, the inertial terms in the Navier-Stokes are negligible. In the following, we solve the Stokes equation using a streamfunction-vorticity formalism. Although we assume the liquid to be incompressible, we take into account temperature variations of the density leading to the steady-state continuity equation

$$\nabla \cdot (\rho \vec{u}) = 0. \tag{9}$$

For this reason, we incorporate the variable density in the definition of the streamfunction ψ. The Cartesian velocity components $\vec{u} = (u_x, u_y)$ are given by

$$u_x = \frac{1}{\rho}\frac{\partial}{\partial y}(\rho\psi), \tag{10}$$

$$u_y = -\frac{1}{\rho}\frac{\partial}{\partial x}(\rho\psi). \tag{11}$$

The viscosity of EG, $\mu = \mu(T)$, also depends on the temperature according to Eq. (B1) (see Appendix B). Introducing ω_z

as the z-component of the vorticity $\vec{\omega} \equiv \nabla \times \vec{u}$, the Stokes equation results in the following coupled second-order equations:

$$\omega_z = -\nabla^2 \psi - \nabla \cdot \left[\frac{\psi}{\rho} \nabla \rho \right], \tag{12}$$

$$\mu \nabla^2 \omega_z = g \frac{\partial \rho}{\partial x} + \cdots$$
$$+ \left(\nabla \left[\nabla^2 \psi \right] \right) \cdot \nabla \mu + \nabla^2 \left(\frac{\psi}{\rho} \nabla \rho \right) \cdot \nabla \mu. \tag{13}$$

For a uniform density, Equations (10)–(13) reduce to $(u_x, u_y) = (\partial \psi / \partial y, -\partial \psi / \partial x)$ and

$$\omega_z = -\nabla^2 \psi, \tag{14}$$

$$\nabla^2 \omega_z = \frac{1}{\mu} \left(\nabla \left[\nabla^2 \psi \right] \right) \cdot \nabla \mu = -\frac{1}{\mu} (\nabla \mu) \cdot \nabla \omega_z. \tag{15}$$

The flow in the liquid wedge is driven by the motion of the PC substrate and the thermocapillary shear stress along the liquid-air interface. The boundary conditions in case of uniform density are given by

$$\psi = 0, \quad \frac{\partial \psi}{\partial y} = U_{\text{sub}} \quad \text{for } (x < 0, y = 0), \tag{16}$$

$$\psi = 0, \quad \omega_z = -\frac{\tau'}{\mu} \quad (x < 0, y = -\tan(\theta_r)x), \tag{17}$$

$$\frac{\partial \psi}{\partial x} = 0, \quad \frac{\partial \omega_z}{\partial x} = 0 \quad \text{for } (x = x_L, y > 0). \tag{18}$$

The solid-liquid interface at $y = 0$ is a streamline, where the value of ψ is arbitrarily set to zero. The horizontal velocity $\partial \psi / \partial y$ is given by U_{sub} [Eq. (16)]. At the left boundary of the liquid wedge at $x = x_L$, we assume that $\partial \omega_z / \partial x$ and the vertical velocity $\partial \psi / \partial x$ are equal to 0 [Eq. (18)]. These correspond to mirror-symmetry conditions for the scalar fields ψ and w_z, which strictly speaking do not apply to the system studied.[56] However, we chose the value of x_L (and similarly of x_R) sufficiently large such that there is no influence of this boundary condition neither on the temperature distribution nor on the velocity field near the contact line. We note that this boundary condition implies the streamlines to be horizontal, i.e., parallel to $\vec{n}$ at $x = x_L$. The liquid-air boundary is also a streamline for a non-volatile liquid. The non-uniform temperature along this boundary results in a thermocapillary shear stress[57]

$$\tau' = \frac{d\gamma}{dT} \vec{t} \cdot \nabla T, \tag{19}$$

due to the temperature dependence of the surface tension. Here, $\vec{t}$ is the tangential unit vector of the computational domain and $d\gamma / dT = -0.089$ mN/(m K) the temperature dependence of the surface tension of EG. We take this shear stress into account by setting the vorticity[58] to $\omega_z = -\tau' / \mu$ [Eq. (17)].

2. Intensity distribution of infrared laser beam

The angle of incidence of the IR laser beam with respect to the PC substrate is kept fixed at $\beta = 45°$ as illustrated in

Fig. 2. We define the intensity profile of the IR laser beam in a separate beam coordinate system (x_b, y_b) illustrated schematically in Fig. 10

$$x_b \equiv (x - d) \cos \beta - y \sin \beta, \tag{20}$$

$$y_b \equiv (x - d) \sin \beta + y \cos \beta. \tag{21}$$

The intensity profile of the IR laser beam is given by

$$I = \frac{\sqrt{2}P}{\sqrt{\pi}w} \exp\left(-2 \frac{x_b^2}{w^2} \right) \exp(F). \tag{22}$$

The width w is given by

$$w = w_0 + |y_b| \tan \theta_d, \tag{23}$$

where $w_0 = 0.6$ mm is the minimum waist width and $\theta_d = 8°$ quantifies the divergence of the laser beam. P is the power per unit length in the z-direction. The last term of Eq. (22), $\exp(F)$, represents the absorption of the beam in the EG wedge, the PC substrate, and the glass plate. The parameter $F = F(\alpha, x_b, y_b, d, \theta_r, \beta, d_{\text{PC}})$ describes the optical path length through these different domains (see Appendix A). Refraction effects and partial reflections at the dielectric interfaces are not taken into account.

B. Contact line displacement model

In order to model the IR laser induced displacement of the contact line, we use the classical, well-studied Landau-Levich[59] dip-coating geometry where a substrate is withdrawn *vertically* from a liquid bath.[60] Figure 3 shows the 1D computational domain for the CL model. The liquid film profile $h(x)$ is governed by the so-called lubrication equation[61]

$$\frac{\partial h}{\partial t} + \frac{\partial}{\partial x} \left(\frac{h^2}{2\mu(T)} \tau - \frac{h^3}{3\mu(T)} \frac{\partial \mathcal{P}}{\partial x} + U_{\text{sub}} h \right) = 0. \tag{24}$$

The augmented pressure

$$\mathcal{P} \equiv -\gamma(T) \frac{\partial^2 h}{\partial x^2} + \rho(T) gx - \Pi(h), \tag{25}$$

represents the influence of capillary pressure, hydrostatic pressure, and the disjoining pressure[62] Π. As the x-dependence of the hydrostatic pressure term in Eq. (25) indicates,

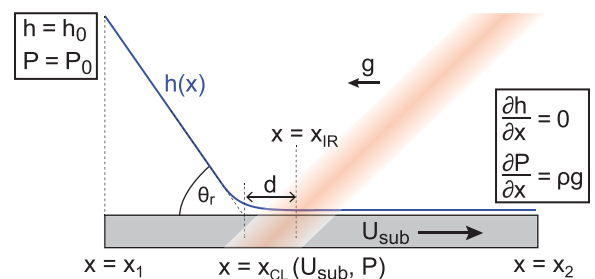FIG. 3. For $x > x_{\text{CL}}$, the film thickness is approximately equal to h^*. Schematic representation of the computational domain and boundary conditions of the contact line model.

the direction of the gravitational acceleration is in the negative x-direction. The viscosity $\mu(T)$, density $\rho(T)$, and surface tension $\gamma(T)$ are given in Appendix B. We use a phenomenological expression for the disjoining pressure[63] Π

$$\Pi(h) = \gamma\left(1 - \cos\theta_{eq}\right)\frac{(n-1)(m-1)}{(n-m)h^*}\left[\left(\frac{h^*}{h}\right)^n - \left(\frac{h^*}{h}\right)^m\right].$$
(26)

The parameters (n, m, h^*) are chosen as $(6, 4, 20\,\text{nm})$. The contact angle θ_{eq} is fixed at $20°$.

We used the following boundary conditions:

$$h(x = x_1) = h_0, \quad \mathcal{P}(x = x_1) = \mathcal{P}_0,$$
(27)

$$\frac{\partial h}{\partial x}(x = x_2) = 0, \quad \frac{\partial \mathcal{P}}{\partial x}(x = x_2) = \rho g.$$
(28)

The width of the computational domain $x_2 - x_1 = 1\,\text{mm}$ is chosen sufficiently large so that it does not influence the CL dynamics. At $x = x_2$, the gradient of the film thickness, $\partial h/\partial x$, is set to 0 and the gradient of the augmented pressure $\partial \mathcal{P}/\partial x$ is set equal to ρg [Eq. (28)]. At $x = x_1$, the film thickness is fixed at $h_0 = 50\,\mu\text{m}$ [Eq. (27)]. The pressure is fixed at the reservoir pressure

$$\mathcal{P}_0 = -\sqrt{2\gamma\rho g(1 - \sin\theta)}.$$
(29)

C. Coupling of the two models

We extract the temperature $T(x)$ and the temperature gradient $\frac{\partial T}{\partial x}(x)$ along the liquid-air interface and the PC-air boundary (as indicated with the green line in Fig. 2) from the heat-transfer model. From the temperature and the temperature gradient, we obtained the temperature dependent material parameters and the thermocapillary shear stress $\tau = (d\gamma/dT)(\partial T/\partial x)$, respectively, for the CL model. The new resulting location of the contact line x_{CL} is defined as the position of maximum curvature $\partial^2 h/\partial x^2$. This position corresponds to $x = 0$ in the heat-transfer model. The parameter x_{CL} is used in the heat-transfer model to update the distance d between the CL and the position of maximum laser intensity x_{IR}. It is also used to update the approximate receding contact angle θ_r

$$\theta_r = \arctan\left(\frac{h_0}{x_{CL} - x_1}\right).$$
(30)

III. RESULTS FROM HEAT-TRANSFER MODEL

In order to illustrate typical behavior, we first present results of the heat-transfer model alone, i.e., we keep the values of d and θ_r fixed and do not consider the coupling with the CL model. Moreover, we first solved Eqs. (1), (12), and (13) for several representative cases. It turned out that the effect of thermal expansion, i.e., a non-uniform density $\rho(T)$, was negligibly small. Consequently, we assumed ρ to be constant and all results presented correspond to solutions of Eqs. (1), (14), and (15). Figure 4(a) shows the magnitude of
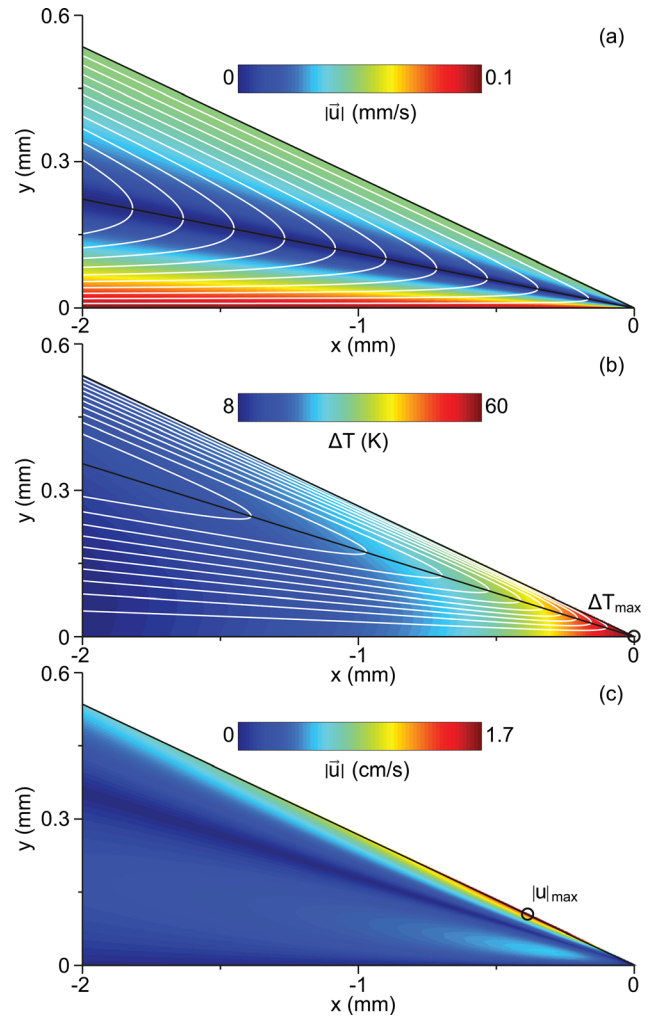

FIG. 4. Numerical results of the heat-transfer model for parameters $U_{sub} = 0.1\,\text{mm/s}$, $d = 0.2\,\text{mm}$, and $\theta_r = 15°$. For simplicity, we set the angle of incidence β and the divergence angle θ_d to 0. Furthermore, we assumed that the thickness of the PC substrate is $d_{PC} = 4.4\,\text{mm}$ and that the glass plate is absent, i.e., $d_{glass} = 0\,\text{mm}$. (a) Pseudo-color plot of the magnitude of the velocity $|\vec{u}|$ in the liquid wedge for $P = 0\,\text{W/m}$. (b) Pseudo-color plot of the temperature increase $\Delta T(x, y) = T(x, y) - T_0$ in the liquid wedge for $P = 500\,\text{W/m}$. The white lines in (a,b) represent the streamlines. (c) Pseudo-color plot of the magnitude of the velocity $|\vec{u}|$ in the liquid wedge for $P = 500\,\text{W/m}$.

the velocity vector $|\vec{u}|$ in the liquid wedge, in the *absence* of laser illumination, i.e., $P = 0\,\text{W/m}$. The white lines represent the streamlines of the flow field. For validation, we compared our numerical results with the analytical solutions for the isothermal flow in a corner by Moffatt[64] with and without the presence of a constant shear stress along the liquid-air interface, τ', and obtained perfect agreement. The black lines in Figs. 4(a) and 4(b) represent the locations where the radial velocity vanishes $u_r = 0$, i.e., the turning points of the streamlines. The radial velocity is defined as $u_r = u_x \cos\varphi + u_y \sin\varphi$, where φ is the polar angle.

Figure 4(b) shows an example of the temperature increase $\Delta T(x, y) \equiv T(x, y) - T_0$ in the liquid wedge for a low substrate speed $U_{sub} = 0.1\,\text{mm/s}$. The white lines represent the streamlines of the flow field. The temperature increases along the liquid-air boundary towards the CL. We observed that the point of maximum temperature rise

(indicated with a circle in Fig. 4(b)) coincides with the CL position up to a speed of approximately 0.4 mm/s. The spacing of the streamlines indicates that the flow speed along the liquid-air boundary is larger than the flow speed along the liquid-substrate boundary. As a consequence, the position of the $u_r = 0$ line is elevated compared to Fig. 4(a). This is illustrated more clearly in Fig. 4(c), where we present the magnitude of the velocity vector $|\vec{u}|$ in the liquid wedge. It shows a thin region with an increased flow speed adjacent to the liquid-air boundary. The maximum speed in this region $|u|_{\mathrm{max}} \approx 1.7$ cm/s (indicated with a circle in Fig. 4(c)), while the substrate speed is only $U_{\mathrm{sub}} = 0.1$ mm/s. The amplified flow in this region is induced by the thermocapillary shear stress, due to the high temperature gradient along the liquid-air boundary.

Fig. 5(a) shows the temperature increase ΔT for a higher substrate speed $U_{\mathrm{sub}} = 3.2$ mm/s. The temperature rise is now much smaller. The point of maximum temperature rise (indicated with a circle in Fig. 5(a)) is still located along the liquid-air boundary, but now left of the contact line. The streamline pattern is very similar to the isothermal case in Fig. 4(a). Figure 5(b) indicates that the flow speed along the liquid-air boundary is of the same order as U_{sub}. The flow induced by the thermocapillary shear stress at the liquid-air boundary is clearly visible, in the vicinity of the point of maximum $|\vec{u}|$ (indicated with a circle in Fig. 5(b)).

The red circles in Fig. 6 (left axis) show the ratio $|u|_{\mathrm{max}}/U_{\mathrm{sub}}$ as a function of U_{sub}, where $|u|_{\mathrm{max}}$ is the maximum speed along the liquid-air boundary. The blue diamonds (right axis) indicate the maximum temperature rise ΔT_{max} along the liquid-air boundary. For "low" values of the

FIG. 6. Left axis: $|u|_{\mathrm{max}}/U_{\mathrm{sub}}$ as a function of U_{sub}, where $|u|_{\mathrm{max}}$ is the maximum speed along the liquid-air boundary. The dashed, horizontal line represents Eq. (32). Right axis: Maximum temperature rise ΔT_{max} along the liquid-air boundary as a function of U_{sub}.

substrate speed $U_{\mathrm{sub}} \lesssim 0.05$ mm/s, ΔT_{max} is approximately independent of U_{sub}. Since the position of maximum temperature rise is the CL position for low U_{sub}, the relevant velocity scale is U_{sub} and the relevant length scale is determined by the heat source, i.e., $2w$. Therefore, the appropriate definition of the Peclet number is given by $Pe_w = 2U_{\mathrm{sub}}\rho_{\mathrm{EG}}c_{\mathrm{p,EG}}w/k_{\mathrm{EG}}$. Pe_w assumes a value of 1 for $U_{\mathrm{sub}} = 0.08$ mm/s, which agrees well with the transition value of 0.05 mm/s observed in Fig. 6. For low U_{sub}, the thermocapillary shear stress τ' also does not depend on U_{sub}. This shear stress is the dominant driving force for the flow, since $|u|_{\mathrm{max}}/U_{\mathrm{sub}} \gg 1$. As a result, also $|u|_{\mathrm{max}}$ is constant in this regime and $|u|_{\mathrm{max}}/U_{\mathrm{sub}}$ scales as $1/U_{\mathrm{sub}}$. For "intermediate" values of U_{sub}, both ΔT_{max} and τ' decrease with increasing U_{sub}. In this regime, $|u|_{\mathrm{max}}$ decreases with increasing U_{sub} and thus $|u|_{\mathrm{max}}/U_{\mathrm{sub}}$ scales as $U_{\mathrm{sub}}^{-\xi}$ with $\xi > 1$. For "high" values of U_{sub}, $|u|_{\mathrm{max}}/U_{\mathrm{sub}}$ approaches a steady-state value ϵ, i.e., $|u|_{\mathrm{max}} = \epsilon U_{\mathrm{sub}}$. In this regime, the motion of the substrate is the dominant driving force for the flow in the wedge and not the temperature gradient along the liquid-air boundary. In general, the thermocapillary flow speed U_{tc} can be estimated as

$$\frac{h}{2\mu}\tau \approx \frac{w\tan\theta_r}{2\mu}\frac{d\gamma}{dT}\frac{\Delta T_{\mathrm{max}}}{w} \approx \frac{1}{2\mu}\tan\theta_r\frac{d\gamma}{dT}\Delta T_{\mathrm{max}}. \quad (31)$$

Since $Pe_w \gg 1$ in this regime, the maximum temperature rise is determined by convective effects and scales approximately as $1/U_{\mathrm{sub}}$. Approximating the typical temperature rise with $\Delta T_{\mathrm{max}} \approx C/U_{\mathrm{sub}}$, we can estimate the value of the constant to be $C \approx 40$ K mm/s from the blue curve in Fig. 6. At the transition point where $|u|_{\mathrm{max}}/U_{\mathrm{sub}}$ approaches the constant ϵ, U_{tc} and U_{sub} by definition are of the same order. Therefore, Eq. (31) results in $U_{\mathrm{sub}} = \sqrt{(1/2\mu)\tan\theta_r(d\gamma/dT)C} \approx 5$ mm/s. This agrees well with the transition observed in Fig. 6.

Using the analytic solution for the flow in the wedge (in case of constant viscosity and no shear stress),[64] it can be shown that
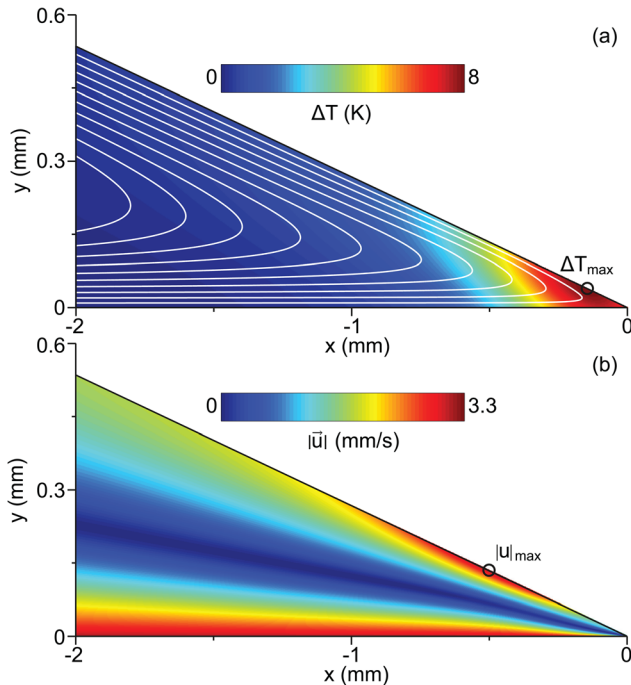

FIG. 5. Numerical results of the heat-transfer model ($U_{\mathrm{sub}} = 3.2$ mm/s, $P = 500$ W/m, $d = 0.2$ mm, $\theta_r = 15°$, $\beta = 0$, $\theta_d = 0$, $d_{\mathrm{PC}} = 4.4$ mm, and $d_{\mathrm{glass}} = 0$ mm). (a) Pseudocolor plot of the temperature increase $\Delta T(x,y)$ in the liquid wedge (the white lines represent the streamlines). (b) Pseudocolor plot of the magnitude of the velocity $|\vec{u}|$ in the liquid wedge.
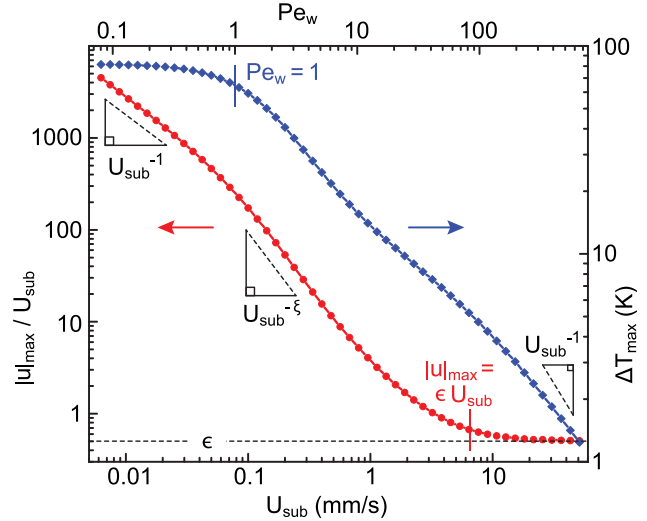
$$\epsilon = \frac{\sin(\theta_r) - \theta_r \cos(\theta_r)}{\theta_r - \sin(\theta_r)\cos(\theta_r)}. \tag{32}$$

The dashed line in Fig. 6 represents Eq. (32).

Figure 7(a) shows the temperature distribution ΔT along the liquid-air boundary and the top boundary of the PC substrate (indicated by the green line in Fig. 2) for different values of d. When $d \gtrsim w_0$, there is no absorption of the IR laser intensity in the EG wedge. In this case, the temperature increases smoothly with x and reaches a steady value when $x > d + w_0$. When $d \lesssim w_0$, part of the IR laser intensity is directly absorbed in the liquid. The temperature rise increases, since $\alpha_{EG} \gg \alpha_{PC}$. The temperature distribution displays a local maximum along the liquid-air boundary left of the contact line, for $d < 0.4\,\text{mm}$.

Figure 7(b) shows the temperature distribution $\Delta T(x)$ for different values of the absorption coefficient of the liquid α_{liq} ($d = 0.2\,\text{mm}$). For comparison, the absorption coefficient of water[65] for an IR wavelength $\lambda = 1470\,\text{nm}$ is $\alpha_{H_2O} = 3100\,\text{m}^{-1}$. When $\alpha_{liq} \lesssim \alpha_{PC}$, the temperature smoothly increases towards the contact line along the liquid-air boundary. For higher values of α_{liq}, the temperature distribution again displays a local maximum along the liquid-air boundary.

Figure 7(c) shows the temperature distribution $\Delta T(x)$ for different values of the laser power P. The temperature rise is approximately linear with the laser power.

For "high" values of U_{sub} (i.e., when the flow induced by the thermocapillary shear stress is negligible), the temperature rise increases with increasing θ_r (data not shown). With increasing θ_r, the liquid wedge absorbs a larger fraction of the incident IR laser intensity. For "low" values of U_{sub} (i.e., when the flow induced by the thermocapillary shear stress is dominant), the temperature rise decreases with increasing θ_r (data not shown). The convection of heat away from the contact line increases with increasing θ_r, thus lowering the temperature rise.

IV. RESULTS FROM COUPLED MODELS

In this section, we present results from the coupled heat-transfer and CL displacement models. Figure 8(a) shows the receding contact angle θ_r (determined from the moving contact line model) as a function of U_{sub}. The red circles are obtained for the case of no laser heating, i.e., $P = 0\,\text{W/m}$. We assume that the temperature and thus the material parameters are uniform and $\tau = 0$. θ_r decreases with increasing U_{sub}. Beyond a critical value of $U_{sub} \approx (1.65 \pm 0.05)\,\text{mm/s}$, it is no longer possible to find a steady state value of θ_r. For substrate speeds higher than this value, a Landau-Levich film is deposited on the substrate. When the laser is switched on, we assume that the material parameters $\mu(T)$, $\rho(T)$, and $\gamma(T)$ depend on the local temperature and we include the thermocapillary shear stress τ from the heat-transfer model. The location of maximum laser intensity in the contact line model is $x_{IR} - x_1 = 0.43\,\text{mm}$. When the laser power is increased to $P = 500\,\text{W/m}$, the green triangles in Fig. 8(a)
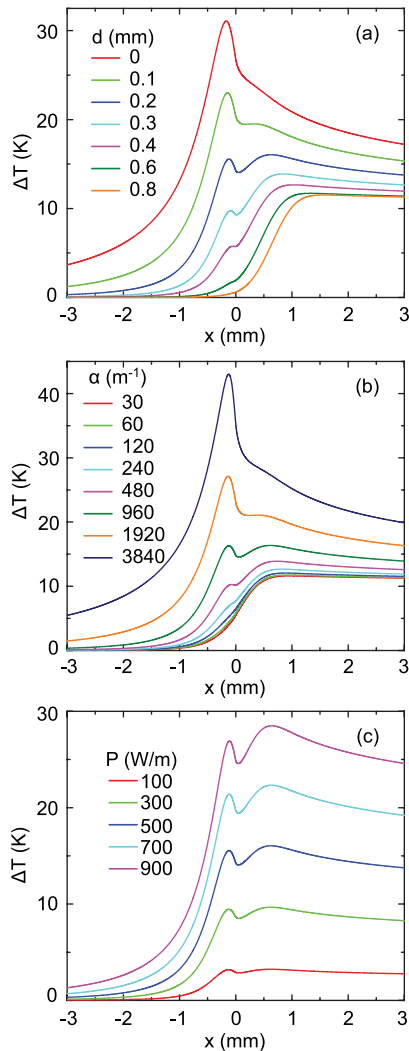

FIG. 7. Temperature distribution $\Delta T = T(x) - T_0$ along the liquid-air boundary and the top boundary of the PC substrate. (a) $\Delta T(x)$ for different values of d (with $U_{sub} = 0.8\,\text{mm/s}$, $P = 500\,\text{W/m}$, and $\theta_r = 15°$). (b) $\Delta T(x)$ for $d = 0.2\,\text{mm}$ and different values of the absorption coefficient α_{liq}. (c) $\Delta T(x)$ for $d = 0.2\,\text{mm}$ and different values of the laser power P.
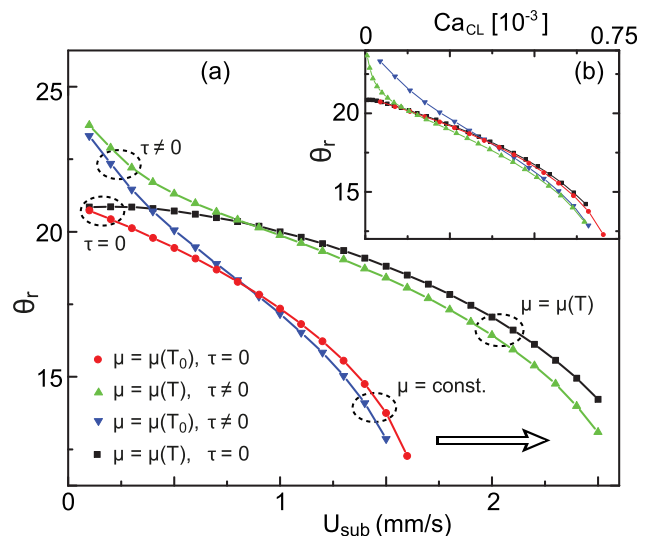
FIG. 8. (a) Receding contact angle θ_r as a function of U_{sub} for $P = 500\,\text{W/m}$ and $x_{IR} - x_1 = 0.43\,\text{mm}$. Red circles: Constant material parameters, thermocapillary effects not included, $\tau = 0$. Green triangles: Variable material parameters, $\tau \neq 0$. Blue triangles: Constant material parameters, $\tau \neq 0$. Black squares: Variable material parameters, $\tau = 0$. (b) Receding contact angle θ_r as a function of Ca_{CL}.

are obtained. The critical speed $U_{sub} \approx (2.57 \pm 0.06)$ mm/s is now more than 50% higher. Moreover, θ_r strongly increases for low U_{sub} compared to the case of $P = 0$ W/m.

In order to identify the dominant mechanisms behind the increase in critical speed and the overall increase in θ_r, we performed separate series of simulations where we neglected either the temperature dependency of the viscosity or the effect of the thermocapillary shear stress τ. The blue triangles in Fig. 8(a) correspond to the case of uniform viscosity, $\mu = \mu(T_0)$ but the influence of τ is taken into account in the CL model. The black squares in Fig. 8(a) correspond to the case of temperature dependent viscosity, $\mu = \mu(T)$ but the influence of τ is not taken into account in the CL model. In the heat-transfer model, however, we include τ' and assume the material parameters are variable in all cases.

The comparison of the green and black, as well of the blue and red curves, shows that the increase in θ_r for low U_{sub} is caused by the thermocapillary shear stress. For the black squares, we do not include τ and we retrieve the same θ_r as for the red circles in the limit $U_{sub} \rightarrow 0$. For low U_{sub}, the maximum temperature rise occurs at the location of the contact line. The shear stress is thus always directed *away* from the contact line, which causes the increase of θ_r for low U_{sub}. The blue triangles show that for increasing U_{sub} the effect of the thermocapillary shear stress diminishes, since the magnitude of τ itself decreases. For sufficiently high speeds, θ_r can even be lower than the laser-off case ($P = 0$ W/m, red line). In this regime, the maximum temperature rise occurs left of the location of the contact line. The shear stress is thus directed *towards* the contact line, which decreases θ_r. A steady-state value of θ_r can be found up to $U_{sub} \leq 1.5$ mm/s. The influence of the shear stress on the critical speed is thus quite small.

The black squares show the effect of temperature dependent viscosity. In this case, a steady-state value of θ_r was found up to $U_{sub} \leq 2.5$ mm/s. The critical speed increased by more than 50% relative to the red curve.

Figure 8(b) shows the receding contact angle θ_r as a function of the capillary number of the contact line $Ca_{CL} \equiv \mu(T_{CL}) U_{sub} / \gamma(T_{CL})$. Here, T_{CL} is the temperature at the contact line. The curves correspond to the same contact angle data sets θ_r as the curves in Fig. 8(a), but plotted as a function of Ca_{CL}. For the red circles and blue triangles, T_{CL} corresponds to the initial temperature T_0. The curves essentially overlap for sufficiently high values of U_{sub}, corroborating the conclusion that reduction of viscous friction is the dominant phenomenon in this regime. The fact that utilization of the capillary number *at the CL position* collapses the curves is a consequence of the fact that the viscous stress exhibits a strong local maximum there.

An equivalent point of view is provided by a comparison of the magnitudes of the thermocapillary and the total viscous shear stress

$$\mu \frac{\partial u_x}{\partial y}(y = 0) = -\frac{\partial \mathcal{P}}{\partial x} h + \tau. \qquad (33)$$

In the limit $U_{sub} \rightarrow 0$, the total viscous shear stress is dominated by the thermocapillary contribution. In contrast, for

$U_{sub} \gtrsim 1$ mm/s in Fig. 8(a), the first term on the right hand side of Eq. (33) by far exceeds τ.

Figure 9(a) shows the receding contact angle θ_r as a function of U_{sub} for different values of the laser power P. In all cases, the temperature dependence of the material parameters and the thermocapillary shear stress are taken into account. The increase of θ_r at low values of U_{sub}, caused by the shear stress τ, becomes more prominent for increasing P. The largest value of U_{sub} at which a stationary value of θ_r can be found increases with increasing P. The dotted lines represent polynomial fitting functions of the form

$$C_0 + C_1 \theta_r + C_2 \theta_r^2 + C_3 \theta_r^3 = U_{sub}. \qquad (34)$$

The values of θ_r for low U_{sub}, where the thermocapillary shear stress is dominant, are not included for the fit. We define the critical velocity U_c as the value of U_{sub} where the fitting function has a vertical tangent line, i.e., where $\partial U_{sub} / \partial \theta_r = 0$. Figure 9(b) presents the relative enhancement of the critical speed $U_c/U_c(P = 0)$ as a function of laser power P. Despite the 3D-nature of the experiments and the 2D-nature of the simulations, the relative increase of U_c is of comparable magnitude[66] (see Fig. 7 of Paper I).

V. SUMMARY

We studied the increase in mobility of stationary contact lines on a moving, partially wetting substrate by using infrared laser illumination of its receding contact line. Below a certain critical speed, the receding contact angle maintains a finite, i.e., non-zero value, and no liquid is entrained on the substrate. The transition towards a Landau-Levich film, i.e., residual liquid left behind on the substrate, occurs at the critical speed. We were specifically interested in the increase in critical speed due to the laser irradiation.

We developed a model for the liquid flow and heat transfer in the vicinity of the contact line, where we take into account thermocapillary shear stresses and the temperature induced variation of the liquid density and viscosity. For

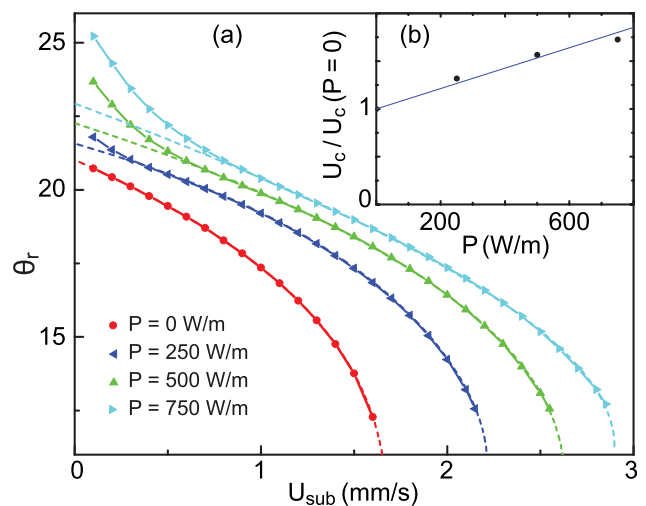

FIG. 9. (a) Receding contact angle θ_r as a function of U_{sub} for different values of the laser power P. The dotted lines represent fitting functions, given by Eq. (34). (b) Relative enhancement of the critical speed U_c as a function of laser power.

values of the substrate speed higher than the critical speed, the flow near the contact line is primarily driven by the motion of the substrate. For values significantly lower than the critical speed, the thermocapillary shear stress is the dominant driving mechanism of the flow.

We developed a second, coupled model to describe the displacement of the receding contact line as a consequence of the laser-induced non-uniform temperature distribution. We found that the thermocapillary shear stress at low substrate speeds is directed away from the contact line and increases the receding contact angle. However, its effect on the critical speed is minimal since the magnitude of the thermocapillary stress diminishes with increasing substrate speed. Thus, the temperature induced decrease of viscosity, i.e., the reduction of the viscous friction, is identified as the dominant mechanism for the increase in critical speed.

The experiments described in Paper I are intrinsically three-dimensional in nature. The receding contact develops a pointed shape for sufficiently high substrate speeds. Although our two-dimensional model does not include this effect, the relative increase in critical speed that we found in the simulations agrees reasonably well with the experimental results for comparable laser intensities.

ACKNOWLEDGMENTS

APPENDIX A: OPTICAL PATH LENGTH

Figure 10 shows a schematic illustration of the laser beam coordinate system (x_b, y_b) and its relation to the coordinate system (x, y) expressed by Eqs. (20) and (21).

In the EG wedge $(x_b < -d \cos \beta)$, the parameter F in Eq. (22) is given by

$$F_{EG} = \alpha_{EG}(y_b - h_1), \tag{A1}$$

where h_1 is given by

$$h_1 = (x_b + d \cos \beta) \tan(\beta - \theta_r) - d \sin \beta. \tag{A2}$$

In the PC substrate, F is given by

$$F_{PC} = \alpha_{EG}(h_2 - h_1) + \alpha_{PC}(y_b - h_2), \tag{A3}$$

where h_1 for $x_b < -d \cos \beta$ is given by Eq. (A2) and for $x_b \geq -d \cos \beta$ by

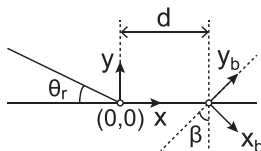$$h_1 = x_b \tan \beta, \quad \text{for } x_b \geq -d \cos \beta, \tag{A4}$$

FIG. 10. Schematic illustration of the laser beam coordinate system.

and h_2 is given by

$$h_2 = x_b \tan \beta. \tag{A5}$$

In the glass plate, F is given by

$$F_g = \alpha_{EG}(h_2 - h_1) - \alpha_{PC}\frac{d_{PC}}{\cos \beta} + \alpha_{glass}(y_b - h_3), \tag{A6}$$

where h_1 is given by Eqs. (A2) or (A4), h_2 is given by Eq. (A5), and h_3 is defined as

$$h_3 = x_b \tan \beta - \frac{d_{PC}}{\cos \beta}. \tag{A7}$$

APPENDIX B: MATERIAL PARAMETERS

We assume the following material parameters: density $\rho_{PC} = 1200$ kg/m^3, $\rho_{glass} = 2550$ kg/m^3, specific heat capacity $c_{p,EG} = 2300$ J/(kg K), $c_{p,PC} = 1240$ J/(kg K), $c_{p,glass} = 750$ J/(kg K), and thermal conductivity $k_{EG} = 0.24$ W/(m K), $k_{PC} = 0.22$ W/(m K), $k_{glass} = 1.0$ W/(m K). The temperature dependent material parameters of EG are given by[67,68]

$$\mu[\text{mPa s}] = \exp\left(-3.61 + \frac{986.52}{\Delta T + 127.86}\right), \tag{B1}$$

$$\gamma[\text{mN/m}] = 50.21 - 0.09\Delta T, \tag{B2}$$

$$\rho[\text{kg/m}^3] = 1127.68 - 0.66\Delta T - 6.2 \cdot 10^{-4}(\Delta T)^2, \tag{B3}$$

where $\Delta T \equiv T - 273$ K is the temperature in degrees Celsius and T is the absolute temperature in Kelvin.

[1] Y. I. Frenkel, "On the behavior of liquid drops on a solid surface 1. The sliding of drops on an inclined surface," J. Exp. Theor. Phys. **18**, 659 (1948).

[2] Y. Rotenberg, L. Boruvka, and A. W. Neumann, "The shape of nonaxisymmetric drops on inclined planar surfaces," J. Colloid Interface Sci. **102**, 424 (1984).

[3] H.-Y. Kim, H. J. Lee, and B. H. Kang, "Sliding of liquid drops down an inclined solid surface," J. Colloid Interface Sci. **247**, 372 (2002).

[4] S. D. Hong, M. Y. Ha, and S. Balachandar, "Static and dynamic contact angles of water droplet on a solid surface using molecular dynamics simulation," J. Colloid Interface Sci. **339**, 187 (2009).

[5] J. B. Freund, "The atomic detail of a wetting/de-wetting flow," Phys. Fluids **15**, L33 (2003).

[6] J. Hyväluoma, A. Koponen, P. Raiskinmäki, and J. Timonen, "Droplets on inclined rough surfaces," Eur. Phys. J. E **23**, 289 (2007).

[7] P. Roura and J. Fort, "Equilibrium of drops on inclined hydrophilic surfaces," Phys. Rev. E **64**, 011601 (2001).

[8] N. Savva and S. Kalliadasis, "Droplet motion on inclined heterogeneous substrates," J. Fluid Mech. **725**, 462 (2013).

[9] S. P. Thampi, R. Adhikari, and R. Govindarajan, "Do liquid drops roll or slide on inclined surfaces?," Langmuir **29**, 3339 (2013).

[10] K. Ogawa, M. Soga, Y. Takada, and I. Nakayama, "Development of a transparent and ultrahydrophobic glass plate," Jpn. J. Appl. Phys. **32**, L614 (1993).

[11] J. P. Youngblood and T. J. McCarthy, "Ultrahydrophobic polymer surfaces prepared by simultaneous ablation of polypropylene and sputtering of poly(tetrafluoroethylene) using radio frequency plasma," Macromolecules **32**, 6800 (1999).

[12] D. Quéré and M. Reyssat, "Non-adhesive lotus and other hydrophobic materials," Philos. Trans. R. Soc. A **366**, 1539 (2008).

[13] A. Dupuis and J. M. Yeomans, "Dynamics of sliding drops on superhydrophobic surfaces," Europhys. Lett. **75**, 105 (2006).

[14] J. D. Smith, R. Dhiman, S. Anand, E. Reza-Garduno, R. E. Cohen, G. H. McKinley, and K. K. Varanasi, "Droplet mobility on lubricant-impregnated surfaces," Soft Matter **9**, 1772 (2013).

[15] S. Daniel and M. K. Chaudhury, "Rectified motion of liquid drops on gradient surfaces induced by vibration," Langmuir **18**, 3404 (2002).

[16] P. Brunet, J. Eggers, and R. D. Deegan, "Motion of a drop driven by substrate vibrations," Eur. Phys. J.: Spec. Top. **166**, 11 (2009).

[17] J. Hong, S. J. Lee, B. C. Koo, Y. K. Suh, and K. H. Kang, "Size-selective sliding of sessile drops on a slightly inclined plane using low-frequency AC electrowetting," Langmuir **28**, 6307 (2012).

[18] A. A. Darhuber, J. P. Valentino, J. M. Davis, S. M. Troian, and S. Wagner, "Microfluidic actuation by modulation of surface stresses," Appl. Phys. Lett. **82**, 657 (2003).

[19] J. Z. Chen, S. M. Troian, A. A. Darhuber, and S. Wagner, "Effect of contact angle hysteresis on thermocapillary droplet actuation," J. Appl. Phys. **97**, 014906 (2005).

[20] H.-B. Nguyen and J.-C. Chen, "A numerical study of thermocapillary migration of a small liquid droplet on a horizontal solid surface," Phys. Fluids **22**, 062102 (2010).

[21] H.-B. Nguyen and J.-C. Chen, "Numerical study of a droplet migration induced by combined thermocapillary-buoyancy convection," Phys. Fluids **22**, 122101 (2010).

[22] A. L. Yarin, W. Liu, and D. H. Reneker, "Motion of droplets along thin fibers with temperature gradient," J. Appl. Phys. **91**, 4751 (2002).

[23] X. Xu and T. Qian, "Thermal singularity and droplet motion in one-component fluids on solid substrates with thermal gradients," Phys. Rev. E **85**, 061603 (2012).

[24] M. K. Smith, "Thermocapillary migration of a two-dimensional liquid droplet on a solid surface," J. Fluid Mech. **294**, 209 (1995).

[25] H. Liu and Y. Zhang, "Modelling thermocapillary migration of a micro-fluidic droplet on a solid surface," J. Comput. Phys. **280**, 37 (2015).

[26] Y. Sui, "Moving towards the cold region or the hot region? Thermocapillary migration of a droplet attached on a horizontal substrate," Phys. Fluids **26**, 092102 (2014).

[27] G. Karapetsas, K. C. Sahu, K. Sefiane, and O. K. Matar, "Thermocapillary-driven motion of a sessile drop: Effect of non-monotonic dependence of surface tension on temperature," Langmuir **30**, 4310 (2014).

[28] M. L. Ford and A. Nadim, "Thermocapillary migration of an attached drop on a solid surface," Phys. Fluids **6**, 3183 (1994).

[29] S. Mukhopadhyay, N. Murisic, R. P. Behringer, and L. Kondic, "Evolution of droplets of perfectly wetting liquid under the influence of thermocapillary forces," Phys. Rev. E **83**, 046302 (2011).

[30] P. Ehrhard and S. H. Davis, "Non-isothermal spreading of liquid drops on horizontal plates," J. Fluid Mech. **229**, 365 (1991).

[31] V. S. Ajaev, "Spreading of thin volatile liquid droplets on uniformly heated surfaces," J. Fluid Mech. **528**, 279 (2005).

[32] S. W. Benintendi and M. K. Smith, "The spreading of a non-isothermal liquid droplet," Phys. Fluids **11**, 982 (1999).

[33] G. Karapetsas, K. C. Sahu, and O. K. Matar, "Effect of contact line dynamics on the thermocapillary motion of a droplet on an inclined plate," Langmuir **29**, 8892 (2013).

[34] D. M. Anderson and S. H. Davis, "Local fluid and heat flow near contact lines," J. Fluid Mech. **268**, 231 (1994).

[35] V. S. Nikolayev, "Dynamics of the triple contact line on a nonisothermal heater at partial wetting," Phys. Fluids **22**, 082105 (2010).

[36] D. M. Anderson and S. H. Davis, "The spreading of volatile liquid droplets on heated surfaces," Phys. Fluids **7**, 248 (1995).

[37] L. W. Schwartz, D. Roux, and J. J. Cooper-White, "On the shapes of droplets that are sliding on a vertical wall," Phys. D **209**, 236 (2005).

[38] H. Huang and P. Meakin, "Three-dimensional simulation of liquid drop dynamics within unsaturated vertical Hele-Shaw cells," Water Resour. Res. **44**, W03411, doi:10.1029/2007WR006158 (2008).

[39] W.-J. Jeong, M. Y. Ha, H. S. Yoon, and M. Ambrosia, "Dynamic behavior of water droplets on solid surfaces with pillar-type nanostructures," Langmuir **28**, 5360 (2012).

[40] J. H. Snoeijer, B. Andreotti, G. Delon, and M. Fermigier, "Relaxation of a dewetting contact line. Part 1. A full-scale hydrodynamic calculation," J. Fluid Mech. **579**, 63 (2007).

[41] G. Delon, M. Fermigier, J. H. Snoeijer, and B. Andreotti, "Relaxation of a dewetting contact line. Part 2. Experiments," J. Fluid Mech. **604**, 55 (2008).

[42] M. Maleki, E. Reyssat, D. Quéré, and R. Golestanian, "On the Landau-Levich transition," Langmuir **23**, 10116 (2007).

[43] S. D. Iliev and N. C. Pesheva, "Dynamic meniscus profile method for determination of the dynamic contact angle in the Wilhelmy geometry," Colloids Surf., A **385**, 144 (2011).

[44] R. V. Sedev and J. G. Petrov, "The critical condition for transition from steady wetting to film entrainment," Colloids Surf. **53**, 147 (1991).

[45] M. Switkes and M. Rothschild, "Immersion lithography at 157 nm," J. Vac. Sci. Technol. B **19**, 2353 (2001).

[46] R. H. French and H. V. Tran, "Immersion lithography: Photomask and wafer-level materials," Annu. Rev. Mater. Res. **39**, 93 (2009).

[47] L. C. Mayo, S. W. McCue, T. J. Moroney, W. A. Forster, D. M. Kempthorne, J. A. Belward, and I. W. Turner, "Simulating droplet motion on virtual leaf surfaces," R. Soc. Open Sci. **2**, 140528 (2015).

[48] U. Thiele, K. Neuffer, M. Bestehorn, Y. Pomeau, and M. G. Velarde, "Sliding drops on an inclined plane," Colloids Surf., A **206**, 87 (2002).

[49] J. M. Gomba and G. M. Homsy, "Regimes of thermocapillary migration of droplets under partial wetting conditions," J. Fluid Mech. **647**, 125 (2010).

[50] Y. Y. Koh, Y. C. Lee, P. H. Gaskell, P. K. Jimack, and H. M. Thompson, "Droplet migration: Quantitative comparisons with experiment," Eur. Phys. J.: Spec. Top. **166**, 117 (2009).

[51] C. R. Glass, K. F. A. Walters, P. H. Gaskell, Y. C. Lee, H. M. Thompson, D. R. Emerson, and X.-J. Gu, "Recent advances in computational fluid dynamics relevant to the modelling of pesticide flow on leaf surfaces," Pest. Manag. Sci. **66**, 2 (2010).

[52] M. L. Cordero, E. Verneuil, F. Gallaire, and C. N. Baroud, "Time-resolved temperature rise in a thin liquid film due to laser absorption," Phys. Rev. E **79**, 011201 (2009).

[53] H. J. Eichler, P. Günter, and D. W. Pohl, *Laser-Induced Dynamic Gratings* (Springer-Verlag, 1986).

[54] P. Schaaf, *Laser Processing of Materials* (Springer-Verlag, 2010).

[55] F. P. Incropera, D. P. DeWitt, T. L. Bergman, and A. S. Lavine, *Principles of Heat and Mass Transfer* (Wiley, 2013).

[56] N. V. Priezjev, A. A. Darhuber, and S. M. Troian, "Slip behavior in liquid films on surfaces of patterned wettability: Comparison between continuum and molecular dynamics simulations," Phys. Rev. E **71**, 041608 (2005).

[57] A. A. Darhuber and S. M. Troian, "Principles of microfluidic actuation by modulation of surface stresses," Annu. Rev. Fluid Mech. **37**, 425 (2005).

[58] C. Pozrikidis, *Introduction to Theoretical and Computational Fluid Dynamics* (Oxford University Press, 1997).

[59] L. Landau and B. Levich, "Dragging of a liquid by a moving plate," Acta Physicochim. URSS **17**, 42 (1942).

[60] In the experiments, the stand-off distance and the equilibrium contact angle of about 40 degrees induce a negative meniscus curvature and corresponding negative capillary pressure that keeps the droplet attached to the concentric needles when the substrate moves. However, the details of the droplet shape are rather intricate as the advancing side of the droplet is pinned to the inner needle and the receding side to the outer needle. Since our models are based on a straight contact line, these geometric details cannot possibly be implemented. Therefore, we decided to use the more elementary and well-studied Landau-Levich geometry of dip-coating, where the surface curvature is well-defined and determined by the liquid material properties. In this model, gravity (oriented parallel to the substrate) keeps the liquid contact line at a finite distance above the reservoir level at subcritical substrate speeds. Gravity induces a negative capillary pressure in the reservoir meniscus that plays the same role as the negative capillary pressure of the gap meniscus in the experiments mentioned above. Since the overall viscous friction is dominated by the contribution from the contact line region and thus by the value of the receding contact angle, the details of the meniscus shape (outside of the contact line region) are not critically important. The orientation of gravity is unimportant for the 2D heat transfer model, as the domain boundaries are undeformable and (as we found) the laser-induced density differences have a negligible effect on the flow field. For these reasons, the orientation of gravity in the models though different from the experiments in Paper I is not essential for the conclusions drawn.

[61] A. Oron, S. H. Davis, and S. G. Bankoff, "Long-scale evolution of thin liquid films," Rev. Mod. Phys. **69**, 931 (1997).

[62] B. V. Deryagin, "The definition and magnitude of disjoining pressure and its role in the statics and dynamics of thin fluid films," Kolloid. Zh. **17**, 205 (1955).

[63] L. W. Schwartz and R. R. Eley, "Simulation of droplet motion on low-energy and heterogeneous surfaces," J. Colloid Interface Sci. **202**, 173 (1998).

[64]H. K. Moffatt, "Viscous and resistive eddies near a sharp corner," J. Fluid Mech. **18**, 1 (1964).

[65]T. P. Otanicar, P. E. Phelan, and J. S. Golden, "Optical properties of liquids for direct absorption solar thermal energy systems," Sol. Energy **83**, 969 (2009).

[66]The horizontal axis of Fig. 9(b) displays the laser power in units of W/m, while in Fig. 7 of Paper I it is in units of W. An obvious choice of the corresponding length scale for the conversion from overall power to power per unit length is the full width at half maximum (FWHM) of the elliptical laser spot along the *z*-direction. The FWHM was determined in Section II A of Paper I to be approximately 4 mm, i.e. 1 W in Fig. 7 of Paper I corresponds to approximately 250 W/m in Fig. 9(b) of Paper II.

[67]T. Sun and A. S. Teja, "Density, viscosity, and thermal conductivity of aqueous ethylene, diethylene, and triethylene glycol mixtures between 290 K and 450 K," J. Chem. Eng. Data **48**, 198–202 (2003).

[68]MEGlobal Group, "*Ethylene glycol product guide*" (2008).

[69]M. A. van den Tempel, H. M. J. M. Wedershoven, J. C. H. Zeegers, M. Riepen, and A. A. Darhuber, J. Appl. Phys. **119**, 084904 (2016).